(Received 7 November 2025, Accepted 27 December 2025, Scheduled 29 January 2026)

Development of Two Port Koch Geometry Inspired Pentagonal MIMO Antenna for n79 NR 5G Sub-6 GHz Band

Ashish Phalswal[1,*], Ved Prakash[1], Sweta Tripathi[1], and Manish Verma[2]

[1] *Department of Electronics and Communication Engineering, Amity University, Haryana, India*
[2] *SCSE, Galgotias University, Greater Noida, UP, India*

ABSTRACT: A two-port coplanar waveguide (CPW) multiple-input multiple-output antenna (MIMOA) based on Koch geometry (KG) with a wide bandwidth and high isolation is proposed in this work. A high-frequency structure simulator (HFSS) is used for performance analysis and parametric optimization. Initially, a CPW-fed circular patch was designed, which was further modified using KG, and a single antenna element (SAE) was designed. A two-port MIMO layout was further designed using the SAE. The proposed MIMOA is designed with a cross slot on an FR4 substrate, which offers a wide bandwidth of 1110 MHz (3.91–5.02 GHz) and works at 4.16 and 4.69 GHz. It exhibits excellent diversity performance with a Channel Capacity Loss (CCL) < 0.4 bits/s/Hz, Envelope Correlation Coefficient (ECC) < 0.25, Diversity Gain (DG) > 9.7, Mean Effective Gain (MEG) $(1, 2) < 1$ dB, Total Active Refection Coefficient (TARC) ≈ -20 dB from port 1 to port 2, and isolation of ≈ 20 dB across the band. The proposed MIMOA offers a high radiation efficiency (η) of $\geq 80\%$ across the entire band. The designed MIMOA was fabricated and tested to validate the simulation results. The proposed MIMOA is useful for 5G communication and covers a frequency ranging from 3.91 GHz to 5 GHz.

1. INTRODUCTION

Modern high-speed communication and radar systems require high throughput, reliability, and spectral efficiency, which have driven advances in antenna technology [1, 2]. Multi-input multiple-output (MIMO) technology in antenna design plays a vital role in meeting these demands, making this technology indispensable for present-day and next-generation communication systems [3, 4]. 5G communication operating in the n79 5G NR band (4.4–5.0 GHz) supports low-latency and ultra-reliable communication, and requires a compact MIMOA with a wide operating bandwidth and high isolation. Similarly, radar altimeters operating in 4.2–4.4 GHz frequency range are crucial for determining the altitude of the aircraft, and they require robust communication that can be achieved using MIMO technology [5]. MIMOAs use multiple antennas at both the receiving and transmitting sides, which helps improve the channel capacity without the use of extra power and bandwidth [6, 7]. However, MIMOA for the desired applications with high isolation, required bandwidth, low CCL, and high efficiency is a challenging task, particularly when the overall antenna size is small [8, 9].

Innovative techniques are required to implement antenna design to overcome these challenges. Many researchers have recently implemented different approaches in MIMOA design to address these challenges.

The incorporation of fractal structures in a microstrip patch antenna is one of the widely used approaches for achieving multi-band, wideband characteristics, and miniaturization in antenna design [10, 11]. In [1], an MIMOA with a semi-circular cut on a corner and defected in the ground was proposed for the 5G and 6G bands. In this design, a special structure in the connected ground was used to improve isolation. In [2], a two-port Koch Fractal Geometry (KGF) MIMOA with a multilayer structure was proposed. The proposed MIMOA has a size of $60 \times 59.8 \times 1.6\,\text{mm}^3$, and it operates at 2.85, 4.75, 6.30, and 7.81 GHz with a maximum isolation of $\approx$25 dB. In [12], a two-element MIMOA for WLAN and 5G sub-6 GHz applications was designed with a size of $0.30\lambda \times 0.51\lambda$. It covers frequency from 2.92 to 5.72 GHz and achieved an isolation of 15 dB and a maximum gain of 3 dB. In [13], an array of four elements was initially designed, and later, a four-element array two-port MIMOA was designed for 5G applications on an FR4 substrate with a size of $1.4\lambda \times 1.35\lambda$. The proposed MIMOA covers a frequency range of 3.01–6.5 GHz, maintaining an isolation level of 20 dB. In [14], an MIMOA with two ports was proposed for dual bands, which cover the frequency from 2.5 to 2.7 GHz and 3.4–3.6 GHz, maintaining an isolation level of 25 dB with the help of a metasurface-based structure. In this work, antenna elements with U-shaped slots were used, which were designed on an FR4 substrate with a size of $0.83 - \lambda \times 1.25\lambda$. A particular study [15] examined the design of an MIMOA with two elements, incorporating inverted T- and E-shaped elements. To improve isolation, a parasitic resonator was used in the design. However, the isolation was improved to a limited extent of 20 dB.

In [16], a two-port MIMOA was designed on an FR4 substrate having a size of $0.7\lambda \times 0.5\lambda \times 0.0267\lambda$ and operates from 3 to 7 GHz. The antenna has an isolation level of 15 dB with the help of parasitic elements, and it covers the NR 5G Sub-6 GHz applications. In [17], another study, a two-port MI-

* Corresponding author: Ashish Phalswal (ashishphalswal@yahoo.in).

MOA was proposed with an array structure of four elements. The proposed design has a size of $3.04\lambda \times 4.34\lambda$ and operates from 5.54 to 5.59 GHz. It has two elements arranged orthogonally, containing four elements in each array. The isolation of 30 dB was maintained in operating frequency bands. In [18], a four-port MIMOA was designed based on a half-mode substrate integrated waveguide. It covers the frequency from 5.05 to 5.43 GHz, resonates at 5.35 GHz, and has a size of $1.06\lambda \times 1.06\lambda$. The further exploration of these techniques involved the utilization of two rectangular microstrip lines and a defective ground plane [19]. Additionally, a dual-band MIMO antenna design incorporating L-shaped split-ring resonator-loaded monopole elements was investigated [20]. However, both approaches have limitations in terms of their isolation and compactness. A four-element MIMOA incorporating a decoupling line is reported in [21]. A 30 dB isolation was achieved successfully by utilizing two cross-decoupling lines.

Two studies investigating 1×2 and 2×2 MIMOA systems [22, 23] found that isolation could be improved by simply rotating the unit element, eliminating the requirement of an additional decoupling method. In [24], T- and π-shaped strips were employed to enhance the isolation. One more easily integrated technology, which is also widely used in the literature for improving the overall efficiency, compactness, and high Q, is Substrate Integrated Waveguide (SIW). Some quality works related to SIW technology are as follows. In [25], an eight-port modified-shielded quarter mode (MS-QM) SIW MIMOA for WLAN applications is presented. In this study, SIW technology was used to achieve compactness and isolation. It resonates at 5.5 GHz, with a bandwidth of 170 MHz, size of 54 mm $\times$ 54 mm, gain of 5.5 dB, and isolation of more than 22 dB. Using the same SIW technology, an eight-port MIMOA was presented in [26], in which frequency reconfigurability was achieved using liquid dielectric materials. The MIMOA can be tuned dynamically from 1.29 to 2.51 GHz, and it has a high isolation of more than 28 dB and good radiation characteristics. A self-decoupled two-port MIMO antenna was introduced in [27] for Vehicle-to-Everything (V2X) communication. In this paper, shorting vias are used for creating a weak current region on the ground to achieve a high isolation of 78 dB across the entire operating band with a high gain of 7.4 dB. In another study, an MIMOA with an 8-port configuration was proposed for sub-6 GHz band [28]. It is based on a multiple SIW cavity, which ensures strong field confinement and a good isolation level of 22 dB, and it offers a bandwidth of 220 MHz.

Other approaches for decoupling discussed in the literature involve metamaterials, short-neutral lines [29], grounds with defects, and self-decoupling mechanisms [30–34]. These methods have been developed to improve the isolation of compact MIMOA systems and offer potential solutions to enhance their overall performance.

In this article, an innovative two-port MIMOA based on KG with high isolation is proposed, which resonates at 4.16 and 4.69 GHz. MIMOA shows low ECC, low CCL, high η, and high gain which can be used to achieve high data rates and large channel capacities. A parametrical analysis was carried out to find the optimal dimension for the MIMOA, and different layouts were evaluated to achieve better isolation for the MIMOA. The proposed MIMOA is usable for applications such as: Radar altimeter (4.2–4.4 GHz) and 5G NR n79 band (4.4–5.0 GHz). The proposed antenna has a compact size and wideband operation with good isolation, which are some of the key requirements of the MIMOA used for 5G communication. The major contributions of this study are as follows:

(a) The proposed MIMOA achieves good isolation and a larger bandwidth of 1110 MHz from 3.91 to 5.02 GHz with minimal design complexity compared with [14, 35, 17, 18].
(b) The proposed MIMOA had dimensions of $0.46\lambda \times 0.78\lambda$ (λ — wavelength as per frequency of 3.91 GHz), which is more compact than [2, 13, 14, 35, 17, 18, 22, 36].
(c) The proposed structure has a better diversity performance than [18, 35, 36], which makes it highly suitable for a multipath environment.
(d) The proposed structure obtains an enhanced gain compared with a simple patch antenna resonating at the same frequency.

2. ANTENNA DESIGN

This section describes the path of antenna design from the very beginning CPW Circular Patch Antenna (CPWCA) to two-port multi-input-multi-output antenna (TPMIMOA), including the change of CPWCA to CPW Pentagonal Patch Antenna (CPWPPA) and incorporation of KG into CPWPPA to design SAE. The final section describes the evolution of the TPMIMOA Layout.

2.1. CPW Fed Circular Patch Antenna (CPWCPA) to Single Antenna Element (SAE) Design

Figure 1 shows the CPWCPA design in image (a) at the initial phase, designed on an FR4 substrate with a dielectric constant of 4.4 and height of 1.6 mm at 3.5 GHz using the standard Equation (1) [37, 2] given below:

The effective radius a_{eff} of a circular microstrip patch is:

$$a_{\text{eff}} = a\left[1 + \frac{2h}{\pi a \varepsilon_r}\left(ln\left(\frac{\pi a}{2h}\right) + 1.7726\right)\right]^{1/2} \quad (1)$$

where:

- a = physical radius of the patch,
- h = substrate thickness,
- ϵ_r = relative permittivity of substrate,
- a_{eff} = effective radius used in the resonant frequency equation.

In the next stage, the initial circular patch is transformed into a pentagonal shape, which is called CPWPPA, as shown in image (b) in Figure 1. In the next stage, KG was incorporated into the two edges of the CPWPPA. Fractal geometries have been widely used by researchers to attain miniaturization, wider bandwidth, and multi-frequency behavior characteristics [11, 38–40].

TABLE 1. IFS transformation coefficient.

Map	(a)	(b)	(c)	(d)	(e)	(f)
W_1	0.333333	0.000000	0.000000	0.333333	0.000000	0.000000
W_2	0.166667	−0.288675	0.288675	0.166667	0.333333	0.000000
W_3	0.166667	0.288675	−0.288675	0.166667	0.500000	0.288675
W_4	0.333333	0.000000	0.000000	0.333333	0.666667	0.000000

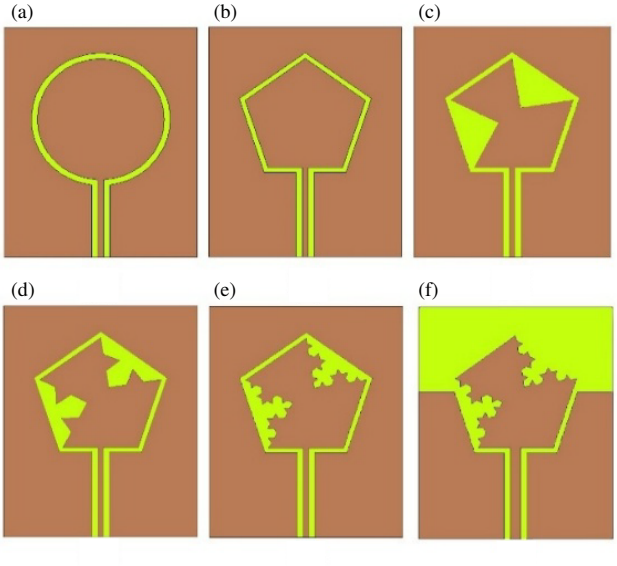

FIGURE 1. Transformation from CPWCPA to SAE. (a) CPWCPA, (b) CPWPPA, (c) 1st Iteration of KG Incorporation, (d) 2nd Iteration KG Incorporation, (e) 3rd Iteration KG Incorporation, (f) SAE Design.

In this study, KG is used to attain a wider bandwidth, and the Koch geometry is shown in Figure 2, whose geometrical descriptors are acquired by the Iterative Fractal System (IFS). The IFS method has been widely used to design a wide variety of usable fractals and has been proven to be an effective design tool. For self-affine fractals, segments are developed at every iteration of the same dimensions and are derived using Equation (2) [41]. Table 1 lists the IFS transformation coefficients of the KG used in the proposed antenna.

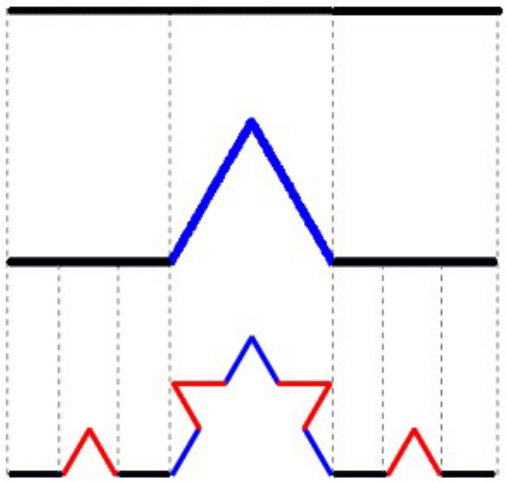

FIGURE 2. Koch geometry (KG).

$$W(x,y) = \begin{bmatrix} a & b \\ c & d \end{bmatrix} \begin{bmatrix} x \\ y \end{bmatrix} + \begin{bmatrix} e \\ f \end{bmatrix} \tag{2}$$

In this design, KG is used up to the 3rd iteration. The design stage shown in image (c) uses the 1st iteration of KG, and the 2nd and 3rd iterations of KG are used in the subsequent stages, as shown in image (d) and (e), respectively. Figure 1 shows the evolution of the SAE from the CPWCPA. Figure 3 shows the dimensional details of the SAE.

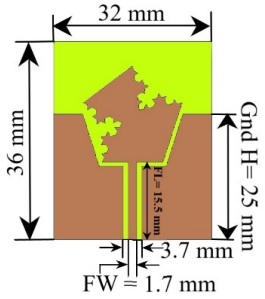

FIGURE 3. SAE design with dimensional details.

The reflection coefficients (S_{11}) of all stages of the design from CPWCPA to SAE are shown in Figure 4. CPWCPA and CPWPPA have similar S_{11} characteristics and operate within a frequency range of 3.25 to 3.61 GHz, offering a bandwidth of 360 MHz. The CPWPPA with the 1st and 2nd iterations of KG have similar circuit characteristics and cover frequency from 2.88 to 3.15 GHz, providing an operating band of 270 MHz. The CPWPPA with the 3rd iteration of KG does not have good matching, and at this stage, antenna design optimization has been performed using parametric optimization. As a result of optimization, the final SAE is evolved from the CPWPPA with the 3rd iteration of KG. During optimization, the ground height (Gnd H) was varied from 13 to 36 mm taking a step size of 2 mm, the Feed Width (FW) varied from 1.5 to 3.0 mm, and the step size kept equal to 0.1 mm. Figure 5 shows a few results from the analysis which are obtained from parametric analysis of the SAE, and from Figure 5, it can be seen that the best results as per requirement are obtained at Gnd H = 25 mm and FW = 1.7 mm. The optimized CPWPPA with the 3rd iteration of KG is named SAE, which offers a bandwidth ranging from 3.91 to 5.02 GHz, resulting in a bandwidth of 1110 MHz. The performance of the design in terms of bandwidth improved is shown in Figure 4. The integration of KG into the CPWPPA changes the Surface Current (SC) distribution, effectively increasing the path length of the current along the surface of the antenna, which results in bandwidth enhancement.

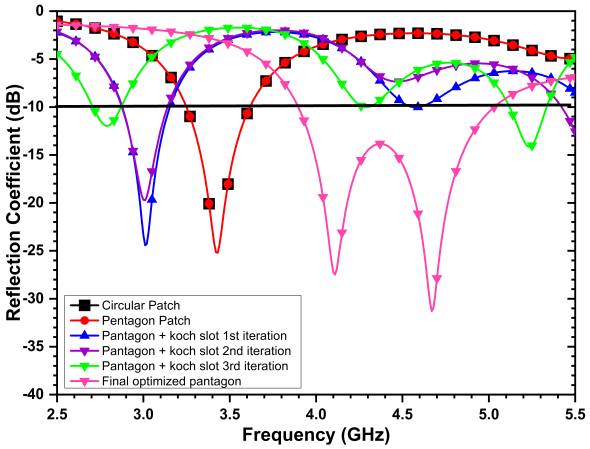

FIGURE 4. S_{11} of CPWCPA and SAE designs.

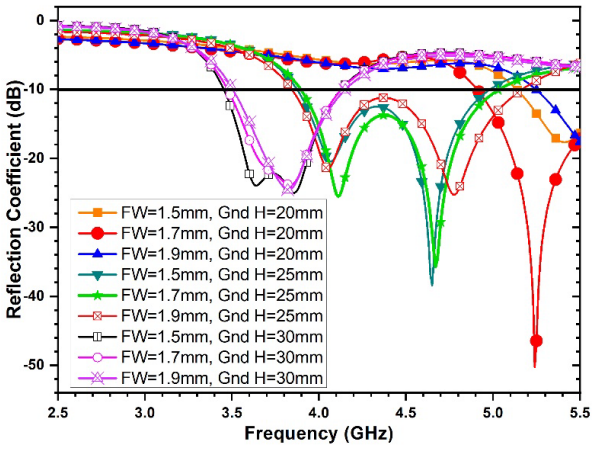

FIGURE 5. Parametric analysis of SAE design at various Gnd H and FW.

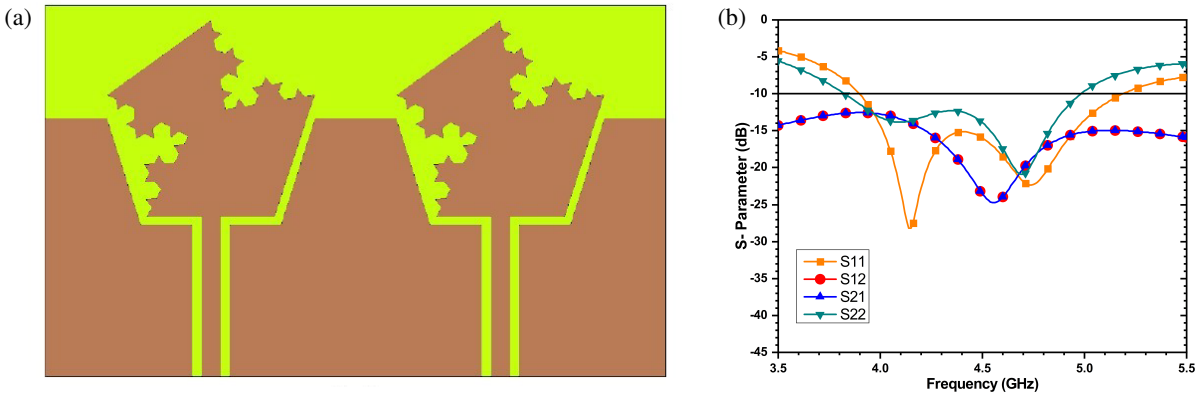

FIGURE 6. TPMIMOA. (a) Layout 1: SAE facing left, (b) SP of Layout 1.

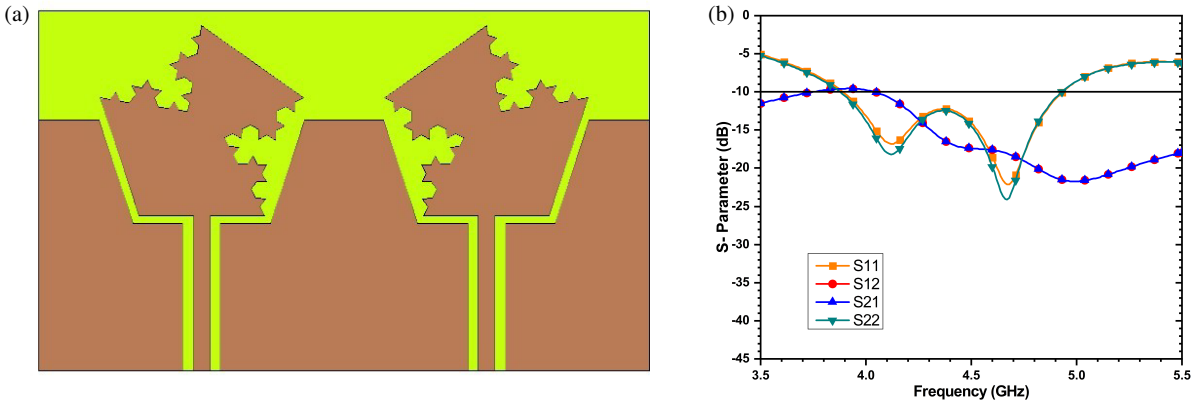

FIGURE 7. TPMIMOA. (a) Layout 2: SAE facing each other, (b) SP of Layout 2.

2.2. TPMIMOA Layout

The SAE was used to design the TPMIMOA after carefully analyzing the results of the SAE in terms of S_{11}. Three different layouts of TPMIMOA were designed using SAE on an FR4 substrate (Dielectric constant $=$ 4.4 and loss tangent $=$ 0.02) with a size of $36 \times 60 \times 1.6\,\text{mm}^3$. Image (a) of Figure 6 shows the layout in which both SAEs face the left side, and its S-parameter (SP) is shown in Figure 6(b). From SP, it can be seen that for this layout, S_{11} and S_{22} are not similar. S_{22} does not cover the required band, and it is below the level of -10 dB up to 4.95 GHz. Therefore, two other layouts, as shown in Figures 7(a) and 8(a), were designed and analyzed. Figure 7(a) shows the layout in which the two SAEs face each other, and the corresponding SP is shown in Figure 7(b). Although S_{11} and S_{22} are very similar in this layout, the isolation among SAEs

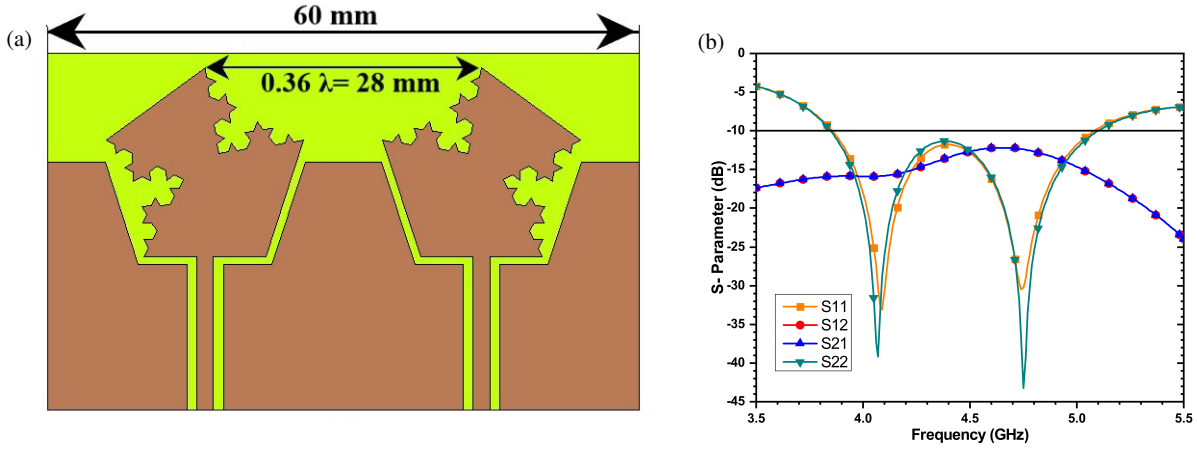

FIGURE 8. TPMIMOA. (a) Layout 3: SAE facing opposite, (b) SP of Layout 3.

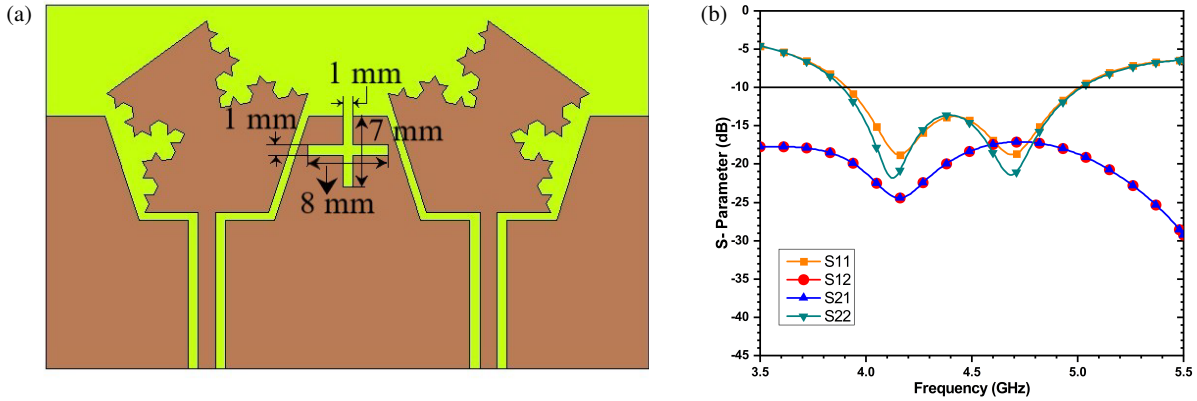

FIGURE 9. Final TPMIMOA (a) Layout 3: SAE facing opposite with cross slot, (b) SP of Layout 3 with cross slot.

is not at an acceptable level, and the available frequency band does not cover up to 5 GHz or the frequency band for targeted applications.

To further examine the TPMIMOA performance, Layout 3 was designed in which the two SAEs face opposite directions, as shown in Figure 8(a). The SP of this layout was analyzed and is shown in image (b) of Figure 8. From all the layouts and their SP, it can be seen that the overall performance of Layout 3, compared to Layouts 1 and 2, exhibits a notable improvement. Layout 3 still needs further improvement in terms of isolation. Although it has achieved the required frequency band, isolation is still not at an acceptable level, and it can be observed that at the second resonant frequency, its isolation is approximately -12 dB. To improve the isolation level throughout the entire operating band, an optimized cross slot was embedded in Layout 3, as shown in Figure 9(a).

The incorporation of a cross-slot configuration, consisting of a 1 mm $\times$ 7 mm vertical slot and a 1 mm $\times$ 8 mm horizontal slot, effectively suppresses surface currents, resulting in an isolation exceeding 18 dB The FW of the 1 $\times$ 2 MIMO antenna layout was again used to optimize the results in terms of the required bandwidth and isolation for the targeted application. The effect of FW variation on bandwidth and matching is analyzed again (from 1.7 mm to 2.5 mm), and an optimum value of 1.9 mm has been selected for further analysis and development of the prototype. Images (a) and (b) in Figure 10 show the SC distribution when port 1 is excited, while port 2 is kept at matched state at 4.16 GHz and 4.69 GHz, respectively, and similarly, images (c) and (d) of Figure 10 show the SC distribution when port 2 is excited, while port 1 is kept at matched state at 4.16 GHz and 4.69 GHz, respectively. When port 1 is excited, the SC density is greater over the surface of the left antenna element. Similarly, when port 2 is excited, the SC density is higher at the right antenna element surface. Moreover, from Figure 9, the effectiveness of the cross slot in the structure can be seen to help in confining the current on the excited antenna element, thus significantly improving the isolation, as shown in Figure 9(b). The effect of KG incorporation can be analyzed from the SC distribution, as this increases the effective path length for the current, thereby enhancing the bandwidth of the antenna.

3. RESULTS AND DISCUSSION

From the different TPMIMOA layouts, Layout 3 was selected for prototyping because the results of Layout 3 were better than those of the other layouts. To verify the circuit and radiation properties, a prototype of the proposed layout of the TPMIMOA, shown in Figure 10(a), was fabricated. SP and radiation

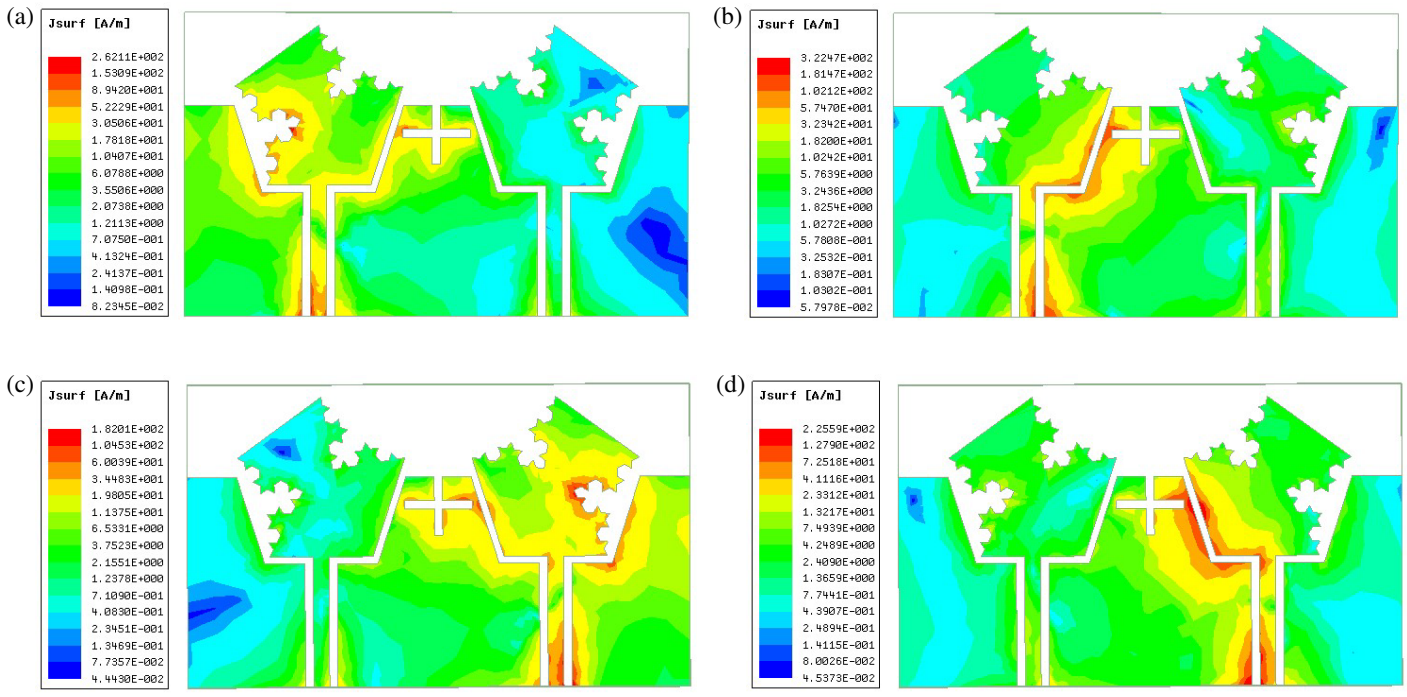

FIGURE 10. SC distributions over the antenna surface in Layout 3. (a) at 4.16 GHz when Port 1 is excited, (b) at 4.69 GHz when Port 1 is excited, (c) at 4.16 GHz when Port 2 is excited, and (d) at 4.69 GHz when Port 2 is excited while the other remains in a matched state.

performance were measured in the laboratory using a Vector Network Analyzer and an anechoic chamber. These laboratory tests provided a thorough evaluation of the circuit and radiation behavior of the proposed TPMIMOA.

Figures 11(a) and 11(b) show the antenna prototype and its view with the anechoic chamber. Figure 11(c) presents the measured and simulated SPs of TPMIMOA across the two ports. The measured parameters were closely aligned with the simulated results, although minor discrepancies were observed. These variations may arise owing to copper loss, slight misalignment of the connector and feed line, fabrication tolerances, and constraints of the laboratory. Minor discrepancies in the bandwidth can be seen in the simulated and measured results, but it does not affect the usability of the TPMIMOA for the targeted application, as it covers the required bandwidth. To determine the practicality of the TPMIMO antenna, several diversity parameters were thoroughly examined. Factors such as mutual coupling, ECC, DG, CCL, and isolation are crucial for determining the capability of a system. A broader understanding of these parameters is a key to designing systems with optimum functionality. The following discussion provides a detailed analysis of these aspects.

3.1. ECC

ECC quantifies the similarity between radiation patterns of the two antennas and helps assess the correlation between the received signal envelopes. A lower ECC value indicates a reduced mutual coupling between the antennas. For optimal MIMOA performance, ECC should be less than 0.5.

It can be calculated using SP and far-field methods [42, 35, 43–45]. Equation (3) is used to calculate the ECC from the SP:

$$ECC = \frac{\left|S_{pp}^{*}S_{pq} + S_{qp}^{*}S_{qq}\right|^{2}}{\left(1 - \left|S_{pp}\right|^{2} - \left|S_{qp}\right|^{2}\right)\left(1 - \left|S_{qq}\right|^{2} - \left|S_{pq}\right|^{2}\right)} \quad (3)$$

Equation (4) given below is used to calculate the ECC from the far field:

$$ECC = \frac{{}_{4\pi}E_{p}\left(\theta, \emptyset\right) \cdot E_{q}\left(\theta, \emptyset\right) d\Omega}{\sqrt{{}_{4\pi}E_{p}\left(\theta, \emptyset\right) \cdot E_{p}^{*}\left(\theta, \emptyset\right) d\Omega \, {}_{4\pi}E_{q}\left(\theta, \emptyset\right) \cdot E_{q}^{*}\left(\theta, \emptyset\right) d\Omega}} \quad (4)$$

where E_p and E_q are the far-field radiation patterns, generated by ports p and q, respectively. The simulated and measured ECCs for the TPMIMOA are depicted in Figure 12, which has a value of less than 0.1 for the entire operating band and confirms that TPMIMOA has a good diversity performance.

3.2. DG

DG measures the improvement in signal quality achieved by using a number of antennas rather than a single antenna. The use of more than one antenna helps the system overcome issues, such as fading and interference, which can degrade the received signal. DG acts as an indicator of how much the signal quality improves because of multiple antennas, with an optimal value generally near 10 dB in the operating region.

A higher DG signifies a better overall system performance. To compute DG, the ECC value is used in Equa-

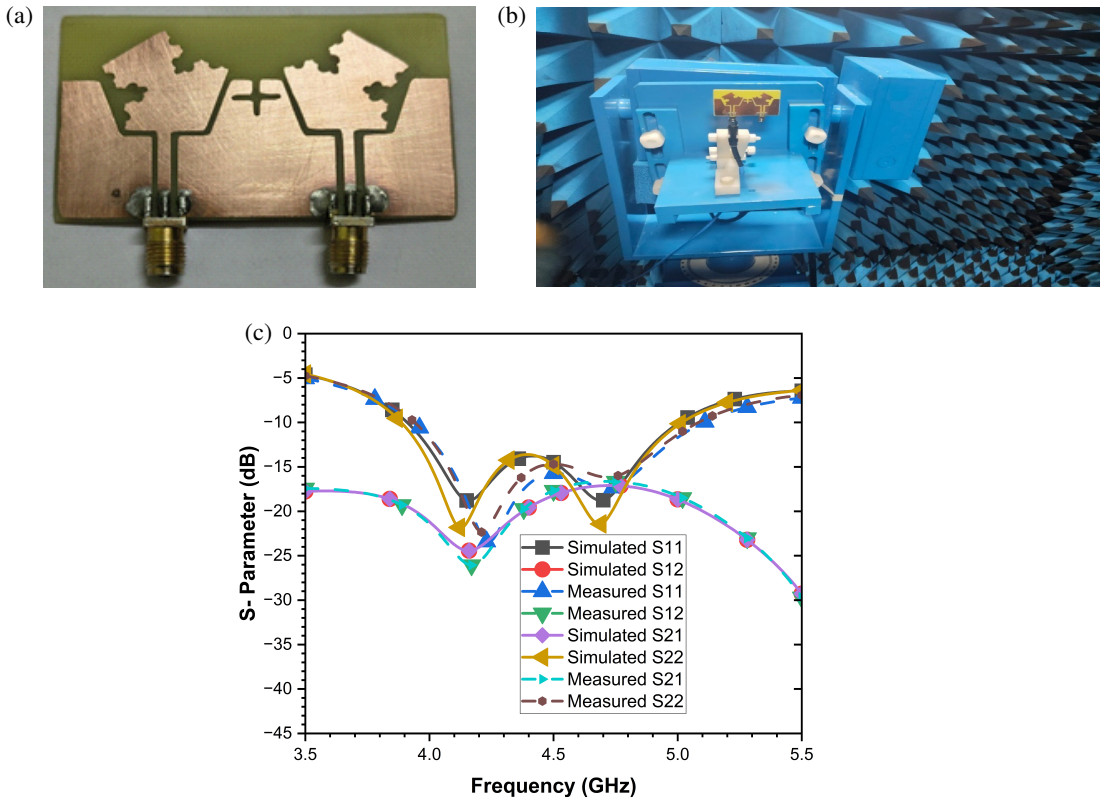

FIGURE 11. (a) Prototype of the TPMIMOA, and (b) Antenna in an anechoic chamber, (c) TPMIMOA SP comparisons between simulated and

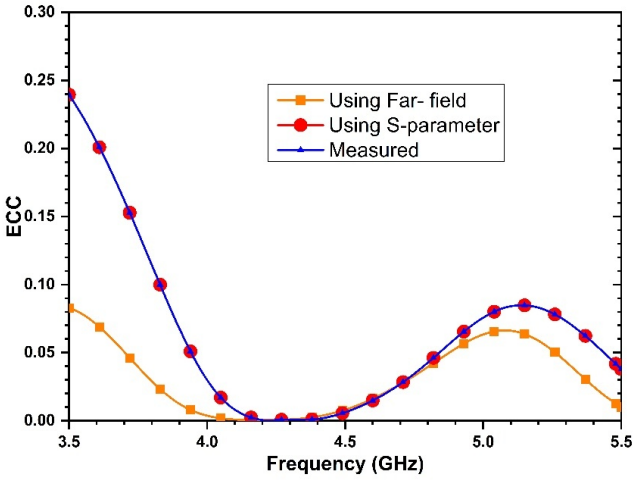

FIGURE 12. ECC for the TPMIMOA.

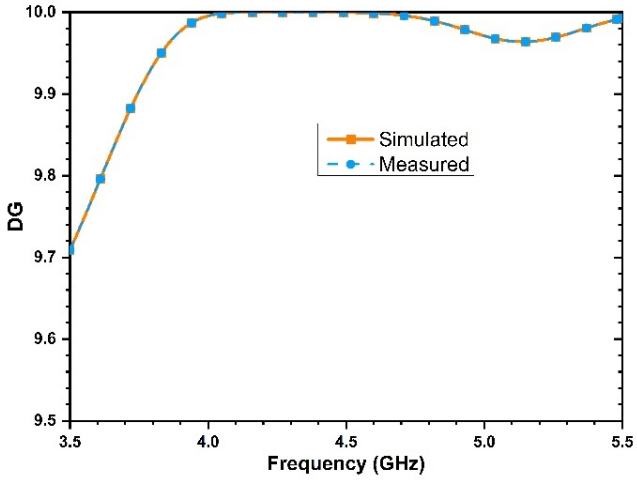

FIGURE 13. DG for the TPMIMOA.

tion (5) [23, 43, 45], as given below:

$$DG = 10 \times \sqrt{1 - |ECC|^2} \tag{5}$$

The simulated and measured DGs for TPMIMOA are above 9.9 dB in the operating region as shown in Figure 13.

3.3. MEG

MEG plays a vital role in designing and analyzing multiple antenna systems, providing valuable information about the overall η, gain, and propagation effects in a multipath fading environment. For an MIMOA system, it should be under -3 dB. In the evaluation of the TPMIMOA system, the simulated and measured MEGs were analyzed, as illustrated in Figure 14, and $MEG(m, n)$ is the ratio of MEGm to MEGn. The MEG is computed using Equations (6) and (7) [23, 44, 45].

$$MEGm = 0.5 \times \left[1 - |S_{mm}|^2 - |S_{mn}|^2\right] \tag{6}$$

$$MEGn = 0.5 \times \left[1 - |S_{mn}|^2 - |S_{nn}|^2\right] \tag{7}$$

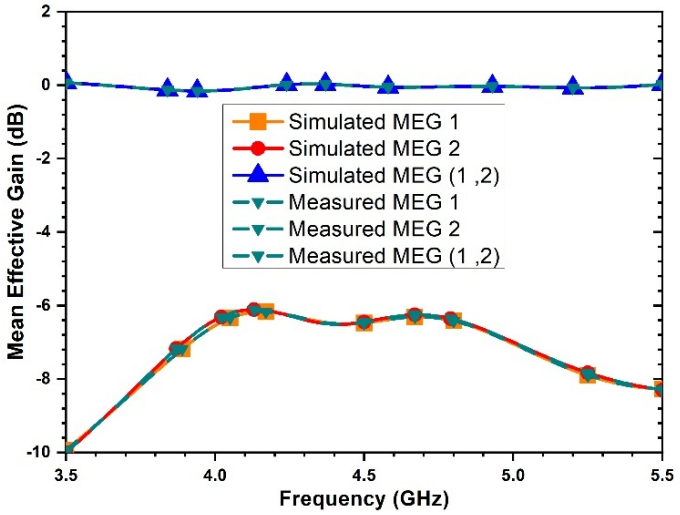

FIGURE 14. MEG of the TPMIMOA.

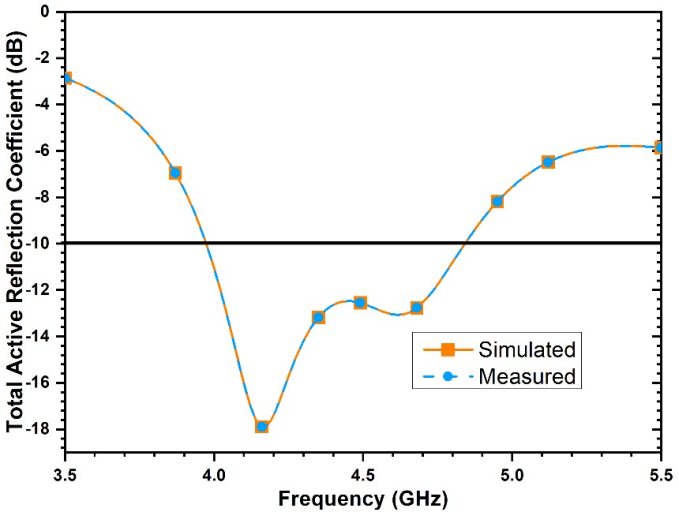

FIGURE 15. TARC of the TPMIMOA.

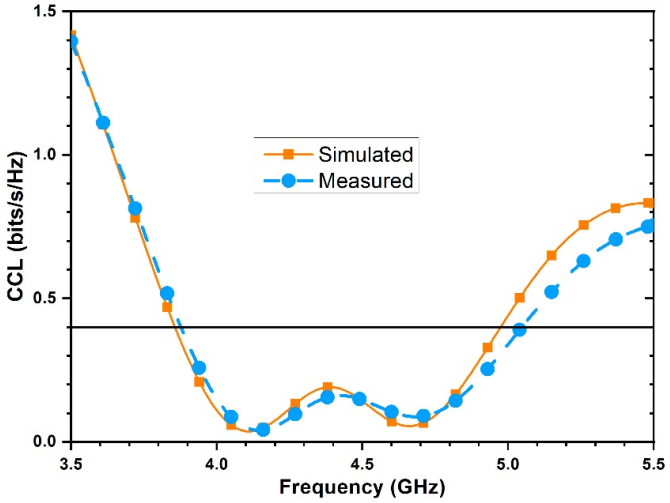

FIGURE 16. CCL of the TPMIMOA.

3.4. TARC

It is the square root of the ratio between the total power reflected and the total incident to all ports and also by using the SP from Equations (8) and (9) [23, 43, 45].

$$TARC = \frac{\sqrt{\sum_{m=1}^{N} |R_m|^2}}{\sqrt{\sum_{m=1}^{N} |I_m|^2}} \tag{8}$$

$$TARC = \sqrt{\frac{|(S_{11} + S_{12}e^{j\theta}|^2 + |(S_{22} + S_{21}e^{j\theta}|^2}{2}} \tag{9}$$

In Equation (8), R_m is the reflected signal, and I_m is the incident signal. To achieve an efficient MIMOA system, the TARC value should remain below -10 dB in the operating band. It can be observed from Figure 15 that the simulated and measured TARC values for ports 1 to 2 of the TPMIMOA are all less than -10 dB.

3.5. CCL

CCL measures the reduction in the highest possible data rate of a communication channel owing to factors such as attenuation, noise, and interference. It indicates a decline in the ability of the system to transmit data efficiently. Understanding the idea of CCL is essential for improving the performance of the system and maximizing η. For MIMOA systems, maintaining the CCL value below 0.4 bits/s/Hz is preferable. The CCL calculation can be performed using Equations (10)–(13) [23, 44] based on the SP. Figure 16 presents the simulated and measured CCL values for TPMIMOA, showing that they remain well below the designated limit of 0.4 bits/s/Hz.

$$CCL = -\log_2 |c^R| \tag{10}$$

$$c^R = \begin{bmatrix} c_{11} & c_{12} \\ c_{21} & c_{22} \end{bmatrix} \tag{11}$$

$$c_{ii} = 1 - \left| \sum_{n=1}^{N} S_{in}^* S_{ni} \right| \tag{12}$$

$$c_{ij} = - \left| \sum_{n=1}^{N} S_{in}^* S_{nj} \right| \tag{13}$$

3.6. Radiation Properties

To verify the simulated results, measurements of the radiation properties of the TPMIMOA were performed in an anechoic chamber. Figure 17 presents the normalized simulated and measured radiation properties in the XZ-plane and YZ-plane, along with 3D-polar plots at 4.16 GHz and 4.69 GHz. The radiation in the YZ-plane demonstrates bidirectional behavior, whereas in the XZ-plane, the TPMIMOA radiates almost uniformly in every direction.

3.7. Gain and Radiation Efficiency (η)

Figure 18 presents the simulated and measured gain plots of the TPMIMOA. It is noted that the maximum gain within the oper-

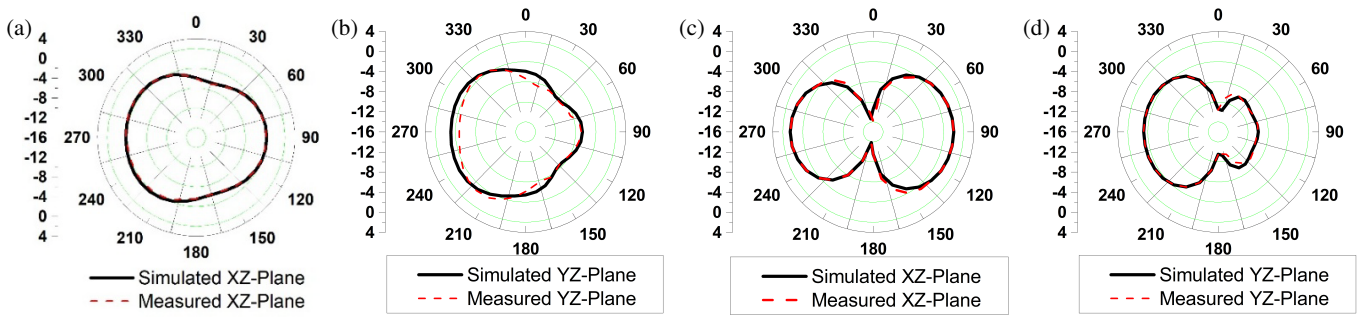

FIGURE 17. Radiation properties of the TPMIMOA. (a) XZ-plane at 4.16 GHz, (b) YZ-plane at 4.16 GHz, (c) XZ-plane at 4.69 GHz, and (d) YZ-plane at 4.69 GHz.

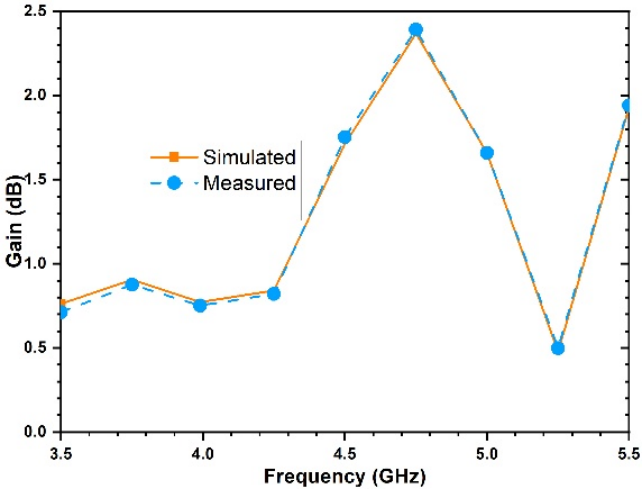

FIGURE 18. Gain plot of TPMIMOA.

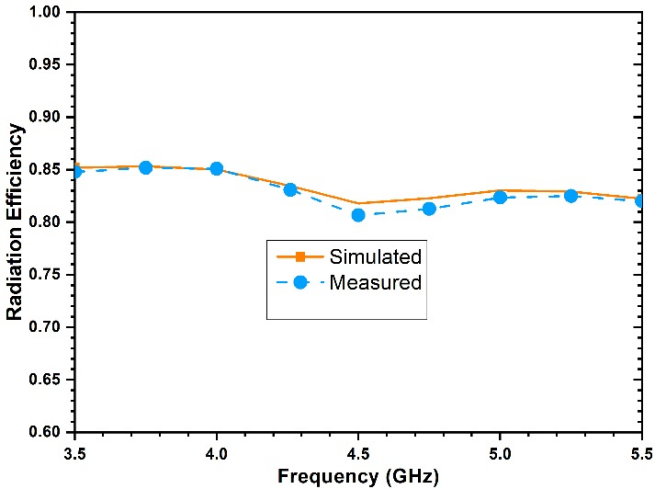

FIGURE 19. Radiation efficiency plot of TPMIMOA.

TABLE 2. Comparison with related work.

Ref. No.	Size (λ^2)	Frequency Range (GHz)	Fractional Bandwidth	Isolation (dB)	ECC
[36]	0.792×0.792	3.3–6.0	58%	15	0.005
[35]	1.7×0.85	3.4–3.6, 4.8–5	5.7%, 4%	16.5	0.01
[2]	0.62×0.61	2.66–3.82, 4.57–4.91, 6.06–6.50, 7.53–8.08	35%, 7%, 7%, 7%	24	< 0.4
[13]	1.4×1.35	3.01–6.5	73%	20	< 0.5
[14]	0.83×1.25	2.5–2.7, 3.4–3.6	7.6%, 5.7%	25	< 0.08
[22]	0.72×0.72	4.3–6.65	43%	20	< 0.004
[23]	0.6×0.6	4.3–6.8	45%	> 20	< 0.2
[18]	1.06×1.06	5.05–5.43	7%	Max. 19.2	< 0.003
[17]	2.98×1.31	5.6–5.67	1.2%	30	0.06
[25]	0.44×0.86	3.2–3.6	$\approx 11\%$	> 25	< 0.05
[27]	–	5.85–6.45	$\approx 9\%$	> 30	< 0.02
[26]	0.19×0.33	1.29–2.51	$\approx 6\%$	> 28	< 0.05
[29]	0.39×0.61	3.296–5.962	57.6%	28 dB (without decoupling) to > 50 dB (with decoupling)	–
Proposed work	0.46×0.78	3.91–5.02	25%	≈ 20	< 0.25

ating range reaches approximately 2.5 dB at 4.75 GHz. In addition, η of the proposed design is more than 80% throughout the operating region as shown in Figure 19. A comparison between TPMIMOA and previous studies from the literature is presented in Table 2. The data clearly indicate that TPMIMOA outperformed its counterparts in terms of performance and size. The

proposed MIMOA achieves a large bandwidth of 1110 MHz from 3.91 to 5.02 GHz with minimal design complexity compared with [14, 35, 17, 18]. It has dimensions of $0.46\lambda \times 0.78\lambda$ (λ — wavelength as per frequency of 3.91 GHz) which is more compact than [2, 13, 14, 35, 17, 18, 22, 36]. The proposed structure has better isolation and diversity performance than those in [18, 35, 36], which makes it highly suitable for multipath environments.

4. CONCLUSION

A KG-inspired CPW-fed TPMIMOA is designed in this work for the 5G Sub-6 GHz band. It provided an impedance bandwidth of 1110 MHz (3.91–5.02 GHz). A cross slot is used in the design, which helps improve the isolation level. The antenna's performance characteristics were extensively analyzed and parametrically optimized to achieve the desired performance. Critical parameters, such as TARC, ECC, CCL, MEG, and DG, were meticulously evaluated to check the MIMOA performance. The simulation results were verified through experimental validation. This detailed analysis of the proposed TPMIMOA demonstrates its suitability for several applications, including 5G communication in the n79 5G NR band and radar altimeters.

ACKNOWLEDGEMENT

The authors sincerely appreciate Amity University Haryana and Galgotias University Greater Noida UP, for valuable research support.

REFERENCES

[1] Kumar, A., A. Kumar, and A. J. A. Al-Gburi, "Development of semi-circular corner cut MIMO antenna for 5G-advanced and 6G automotive wireless applications," *Results in Engineering*, Vol. 25, 103805, Mar. 2025.

[2] Anand, S. and A. Kumar, "Development of two port multilayer MIMO fractal antenna for multiband applications," *Engineering Research Express*, Vol. 7, No. 1, 015369, Mar. 2025.

[3] Irshad Ali, T. K., K. A. Ansal, G. Jagadish Chandran, G. K. Ragesh, and M. Sumitha, "MIMO antenna design for wireless communication: A review on design challenges and isolation techniques," in *2024 1st International Conference on Trends in Engineering Systems and Technologies (ICTEST)*, 01–06, Kochi, India, Apr. 2024.

[4] Anand, S. and A. Kumar, "Multilayer wideband three port CPW multi input multi output antenna for C-band and S-band applications," in *2024 2nd International Conference on Signal Processing, Communication, Power and Embedded System (SCOPES)*, 1–5, Paralakhemundi Campus, Centurion University of Technology and Management, Odisha., India, Dec. 2024.

[5] Kiriş, S. and M. Karaaslan, "An easy-to-produce HIS-based MIMO radio altimeter antenna design for aircraft," *Aircraft Engineering and Aerospace Technology*, Vol. 97, No. 2, 179–189, Jan. 2025.

[6] Kumar Biswas, A. and U. Chakraborty, "Compact wearable MIMO antenna with improved port isolation for ultra-wideband applications," *IET Microwaves, Antennas & Propagation*, Vol. 13, No. 4, 498–504, 2019.

[7] Suresh, A. C., T. S. Reddy, B. T. P. Madhav, S. Das, S. Lavadiya, A. D. Algarni, and W. El-Shafai, "Investigations on stub-based UWB-MIMO antennas to enhance isolation using characteristic mode analysis," *Micromachines*, Vol. 13, No. 12, 2088, Nov. 2022.

[8] Aghoutane, B., S. Das, M. E. Ghzaoui, B. T. P. Madhav, and H. E. Faylali, "A novel dual band high gain 4-port millimeter wave MIMO antenna array for 28/37 GHz 5G applications," *AEU — International Journal of Electronics and Communications*, Vol. 145, 154071, Feb. 2022.

[9] Vasu Babu, K., S. Das, G. Varshney, G. N. J. Sree, and B. T. P. Madhav, "A micro-scaled graphene-based tree-shaped wideband printed MIMO antenna for terahertz applications," *Journal of Computational Electronics*, Vol. 21, No. 1, 289–303, 2022.

[10] Kumar, A. and A. P. S. Pharwaha, "On the design of wideband sierpinski carpet fractal antenna for radio navigation and fixed satellite services," in *2019 6th International Conference on Signal Processing and Integrated Networks (SPIN)*, 736–738, Noida, India, Mar. 2019.

[11] Kumar, A. and A. P. S. Pharwaha, "Dual band minkowski fractal antenna for maritime radio navigation services," *International Journal of Innovative Technology and Exploring Engineering*, Vol. 8, No. 11, 500–505, Sep. 2019.

[12] Nirmal, S., S. Kumar, and R. Chandel, "High isolation compact two port 5G MIMO diversity antenna with asymmetrical feed and partial ground structure," *Progress In Electromagnetics Research C*, Vol. 136, 23–36, 2023.

[13] Ahmed, H., A. M. Ameen, A. Magdy, A. Nasser, and M. Abo-Zahhad, "A sub-6 GHz two-port crescent MIMO array antenna for 5G applications," *Electronics*, Vol. 14, No. 3, 411, Jan. 2025.

[14] Liu, F., J. Guo, L. Zhao, G.-L. Huang, Y. Li, and Y. Yin, "Dual-band metasurface-based decoupling method for two closely packed dual-band antennas," *IEEE Transactions on Antennas and Propagation*, Vol. 68, No. 1, 552–557, Jan. 2020.

[15] Kumar, P. S. and B. C. Mohan, "Design of a compact two element MIMO antenna with improved bandwidth and isolation," in *2015 International Conference on Microwave, Optical and Communication Engineering (ICMOCE)*, 389–392, Bhubaneswar, India, 2015.

[16] Pradeep, P., K. J. Sankar, and C. S. Paidimarry, "Design of a compact wideband two-port MIMO antenna for NR 5G sub-6 GHz band wireless applications," *Wireless Personal Communications*, Vol. 138, No. 2, 1193–1210, Sep. 2024.

[17] Khan, J., S. Ullah, F. A. Tahir, F. Tubbal, and R. Raad, "A sub-6 GHz MIMO antenna array for 5G wireless terminals," *Electronics*, Vol. 10, No. 24, 3062, Dec. 2021.

[18] Wu, T., M.-J. Wang, and J. Chen, "Decoupling of MIMO antenna array based on half-mode substrate integrated waveguide with neutralization lines," *AEU — International Journal of Electronics and Communications*, Vol. 157, 154416, Dec. 2022.

[19] Barani, I. R. R. and K.-L. Wong, "Integrated inverted-F and open-slot antennas in the metal-framed smartphone for 2 × 2 LTE LB and 4 × 4 LTE M/HB MIMO operations," *IEEE Transactions on Antennas and Propagation*, Vol. 66, No. 10, 5004–5012, 2018.

[20] Sarkar, D., K. Saurav, and K. V. Srivastava, "A compact dual band four element MIMO antenna for pattern diversity applications," in *2016 IEEE 5th Asia-Pacific Conference on Antennas and Propagation (APCAP)*, 273–274, Kaohsiung, Taiwan, Jul. 2016.

[21] Rosaline, I., A. Kumar, P. Upadhyay, and A. H. Murshed, "Four element MIMO antenna systems with decoupling lines for high-speed 5G wireless data communication," *Interna-*

tional Journal of Antennas and Propagation, Vol. 2022, No. 1, 9078929, Jun. 2022.

[22] Mohammad Saadh, A. W., S. Khangarot, B. V. Sravan, N. Aluru, P. Ramaswamy, T. Ali, and M. M. M. Pai, "A compact four-element MIMO antenna for WLAN/WiMAX/satellite applications," *International Journal of Communication Systems*, Vol. 33, No. 14, e4506, 2020.

[23] Saadh, A. W. M., P. Ramaswamy, and T. Ali, "A CPW fed two and four element antenna with reduced mutual coupling between the antenna elements for wireless applications," *Applied Physics A*, Vol. 127, No. 2, 88, 2021.

[24] Bai, J., R. Zhi, W. Wu, M. Shangguan, B. Wei, and G. Liu, "A novel multiband MIMO antenna for TD-LTE and WLAN applications," *Progress In Electromagnetics Research Letters*, Vol. 74, 131–136, 2018.

[25] Srivastava, G. and A. Mohan, "Compact eight-port QMSIW cavity-backed MIMO antenna," *IEEE Antennas and Wireless Propagation Letters*, Vol. 23, No. 12, 4044–4048, 2024.

[26] Srivastava, G., A. Kumar, A. Mohan, B. K. Kanaujia, L. Matekovits, and I. Peter, "An eight-port frequency reconfigurable MIMO antenna using liquid dielectrics," *IEEE Access*, Vol. 13, 142 938–142 947, 2025.

[27] Kumar, A., S. Rana, A. Mohan, G. Srivastava, S. Kumar, and K. W. Kim, "A self-decoupled MIMO patch antenna system for V2X communications," *IEEE Access*, Vol. 13, 56 021–56 033, 2025.

[28] Srivastava, G., V. Kumar, and A. Mohan, "Compact 8-port EMSIW MIMO antenna with high isolation for sub-6 GHz communication systems," *International Journal of Microwave and Wireless Technologies*, Vol. 16, No. 10, 1749–1755, 2024.

[29] Babu, K. V., S. Das, S. S. Ali, M. E. Ghzaoui, B. T. P. Madhav, and S. K. Patel, "Broadband sub-6 GHz flower-shaped MIMO antenna with high isolation using theory of characteristic mode analysis (TCMA) for 5G NR bands and WLAN applications," *International Journal of Communication Systems*, Vol. 36, No. 6, e5442, Apr. 2023.

[30] Serghiou, D., M. Khalily, V. Singh, A. Araghi, and R. Tafazolli, "Sub-6 GHz dual-band 8 × 8 MIMO antenna for 5G smartphones," *IEEE Antennas and Wireless Propagation Letters*, Vol. 19, No. 9, 1546–1550, Sep. 2020.

[31] Guo, J., L. Cui, C. Li, and B. Sun, "Side-edge frame printed eight-port dual-band antenna array for 5G smartphone applications," *IEEE Transactions on Antennas and Propagation*, Vol. 66, No. 12, 7412–7417, Dec. 2018.

[32] Sun, L., Y. Li, Z. Zhang, and H. Wang, "Self-decoupled MIMO antenna pair with shared radiator for 5G smartphones," *IEEE Transactions on Antennas and Propagation*, Vol. 68, No. 5, 3423–3432, May 2020.

[33] Xing, H., X. Wang, Z. Gao, X. An, H.-x. Zheng, M. Wang, and E. Li, "Efficient isolation of an MIMO antenna using defected ground structure," *Electronics*, Vol. 9, No. 8, 1265, 2020.

[34] Iqbal, A., O. A. Saraereh, A. Bouazizi, and A. Basir, "Metamaterial-based highly isolated MIMO antenna for portable wireless applications," *Electronics*, Vol. 7, No. 10, 267, Oct. 2018.

[35] Huang, J., G. Dong, J. Cai, H. Li, and G. Liu, "A quad-port dual-band MIMO antenna array for 5G smartphone applications," *Electronics*, Vol. 10, No. 5, 542, Feb. 2021.

[36] Addepalli, T., M. S. Kumar, C. R. Jetti, N. K. Gollamudi, B. K. Kumar, and J. Kulkarni, "Fractal loaded, novel, and compact two-and eight-element high diversity MIMO antenna for 5G sub-6 GHz (N77/N78 and N79) and WLAN applications, verified with TCM analysis," *Electronics*, Vol. 12, No. 4, 952, Feb. 2023.

[37] Balanis, C. A., *Antenna Theory: Analysis and Design*, John Wiley & Sons, 2016.

[38] Kumar, A., B. Dewan, A. Khandelwal, and K. Shrivastava, "On the devolvement of fractal antenna for IoT applications," *Engineering Research Express*, Vol. 5, No. 3, 035026, 2023.

[39] Kumar, A. and A. P. S. Pharwaha, "CPW-fed wide band micromachined fractal antenna with band-notched function," *Applied Computational Electromagnetics Society Journal (ACES)*, Vol. 35, No. 8, 929–935, Aug. 2020.

[40] Kumar, A., A. Kumar, and A. P. S. Pharwaha, "On the development of super-wideband sierpinski triangular fractal antenna," *Wireless Personal Communications*, Vol. 134, No. 1, 119–131, 2024.

[41] Kumar, A. and A. P. S. Pharwaha, "Development of a modified Hilbert curve fractal antenna for multiband applications," *IETE Journal of Research*, Vol. 68, No. 5, 3597–3606, 2022.

[42] Cornelius, R., A. Narbudowicz, M. J. Ammann, and D. Heberling, "Calculating the envelope correlation coefficient directly from spherical modes spectrum," in *2017 11th European Conference on Antennas and Propagation (EUCAP)*, 3003–3006, Paris, France, Mar. 2017.

[43] El Hadri, D., A. Zakriti, A. Zugari, M. E. Ouahabi, and J. E. Aoufi, "High isolation and ideal correlation using spatial diversity in a compact MIMO antenna for fifth-generation applications," *International Journal of Antennas and Propagation*, Vol. 2020, No. 1, 2740920, Jul. 2020.

[44] Abdulkawi, W. M., W. A. Malik, S. U. Rehman, A. Aziz, A. F. A. Sheta, and M. A. Alkanhal, "Design of a compact dual-band MIMO antenna system with high-diversity gain performance in both frequency bands," *Micromachines*, Vol. 12, No. 4, 383, 2021.

[45] He, Z. and J. Jin, "Compact quad-port MIMO antenna with ultra-wideband and high isolation," *Electronics*, Vol. 11, No. 20, 3408, Oct. 2022.